Disturbance-Immune and Aging-Robust Internal Short Circuit Diagnostic for Lithium-Ion Battery

Jian Hu, Hongwen He, *Senior Member, IEEE,* Zhongbao Wei, *Member, IEEE,* and Yang Li, *Member, IEEE*

***Abstract*—The accurate diagnostic of internal short circuit (ISC) is critical to the safety of lithium-ion battery (LIB), considering its consequence to disastrous thermal runaway. Motivated by this, this paper proposes a novel ISC diagnostic method with a high robustness to measurement disturbances and the capacity fading. Particularly, a multi-state-fusion ISC diagnostic method leveraging polarization dynamics instead of the conventional charge depletion is proposed within a model-switching framework. This is well proven to eliminate the vulnerability of diagnostic to battery aging. Within this framework, the recursive total least squares method with variant forgetting (RTLS-VF) is exploited, for the first time, to mitigate the adverse effect of measurement disturbances, which contributes to an unbiased estimation of the ISC resistance. The proposed method is validated both theoretically and experimentally for high diagnostic accuracy as well as the strong robustness to battery degradation and disturbance.**

***Index Terms*—Lithium-ion battery, internal short circuit, fault diagnosis, recursive total least squares, state estimate**

I. INTRODUCTION

LITHIUM-ion batteries (LIBs) have been widely used in electric vehicles (EVs) attributed to the advantages of high power density and long cycling life [1]. However, recently reported fire accidents have attracted public attention over the battery safety problems. The internal short circuit (ISC) is a direct cause of safety hazards of LIBs [2]. Hence, the early-stage ISC diagnostic is of vital importance for the safety management of LIB [3-5].

The ISC diagnostic is a thriving area of research incubating many protocols, classified primarily into four categories including the thermal diagnostic, ancillary circuit measurement, statistical analysis and the model-based approach. In particular, thermal diagnostic lays the foundation on the monitoring of abnormal heating caused by ISC [6], by using specific devices like infra-red imager [7]. Although the direct detection is reliable, the detectable abnormality of heat generation usually means that the thermal runaway has already been initiated. The ancillary circuit methods detect the ISC with special circuit topology in the battery pack [8], and are featured with fast diagnostic. The potential challenge stems from the extra complexity brought to the readily-complicated battery pack.

The statistical approach aims to extract special features from measurements to timely figure out the abnormal cell [9-12]. The micro-short circuit (MSC) was diagnosed in [10] based on the uniform charging cell voltage hypothesis and the variations of remaining charge among cells. A voltage fault diagnostic method was proposed for LIB pack via parameter identification and local outlier detection [11]. A model-free method was proposed in [12] for LIB multi-fault diagnostic including the ISC. Such methods are free from the modeling endeavor by directly analyzing the available measurements. However, elevated uncertainties arise from the multi-cell comparison and the requirement of fully charging.

Depending on the specific model in use, the model-based approaches are divided further into pack model- and cell model-based ones. The short circuit fault was diagnosed online based on a mean-difference pack model (MDM) in [13, 14]. This approach is further extended by incorporating the accurate MDM parameter identification [15]. To evaluate the severity of ISC quantitatively, a MDM-based MSC detection method is proposed by identifying the state of charge (SOC) variation via the extended Kalman filter (EKF) in [16]. A cell difference model (CDM)-based MSC diagnostic method combining low-pass filters is proposed in [17] based on the open circuit voltage (OCV) deviation. These pack model-based methods show expected performance, but uncertainties may arise in practice due to the reliance on the "healthiness" of rest cells and the precise description of both mean cell and the inconsistency.

Alternatively, cell model-based approaches [18-21] utilizes the measurement of single cells, thus are unaffected by rest cells in the pack. In [18], the ISC was diagnosed by online monitoring the parameter change of an equivalent circuit model (ECM) built for the faculty cell. An ISC diagnostic method is proposed in [19] based on SOC estimation and detection of abnormal charge depletion. In spite of the online feasibility, the limited robustness of open-loop architecture potentially declines the ISC detection. An ECM-based hybrid filter is proposed in [21] to identify the model parameters and estimate

Manuscript received September 4, 2020; revised December 22, 2020, January 31, 2021; and February 16, 2021, accepted February 22, 2021. This work was supported by the National Natural Science Foundation of China under Grant 52072038 (Corresponding author: Zhongbao Wei).

J. Hu, H. He, and Z. Wei are with the National Engineering Laboratory for Electric Vehicles, School of Mechanical Engineering, Beijing Institute of Technology, China (e-mail: 3120190329@bit.edu.cn; hwhebit@bit.edu.cn; wzb@bit.edu.cn).

Yang Li is with the Department of Electrical Engineering, Chalmers University of Technology, Sweden (e-mail: yangli@ieee.org).

the ISC resistance simultaneously. It should be noted that most of the quantitative diagnostic methods leverage the abnormal SOC depletion to infer the ISC. The diagnostic hence boils down to the joint estimation of battery states, more particularly, the SOC and parameters of interests. To this end, the model-based SOC estimation has been a vast area of investigation in the past decades showing satisfactory accuracy and robustness [22-24]. Moreover, the parameter identification of LIB is also extensively explored, giving rise to solutions like the population -based [25], regression-based [26-28], and filtering-based techniques [29, 30]. The relevant studies underlie the feasibility of the cell model-based diagnostic methods.

Two major drawbacks are embodied in the aforementioned diagnostic methods. First, the LIB capacity fade also leads to an abnormal SOC depletion which risks invaliding the diagnostic. Second, remarkable disturbances arise from the practical data acquisition due to the quantization noise and the rounding error. The electromagnetic interference also contributes to large noises due to the existence of integrated power electronics and switching devices. Such disturbances impact the diagnostic adversely, which is however less explored. Aimed to bridge this gap, this paper proposes an aging-robust and disturbance-immune ISC diagnostic method. The essence is to transform the ISC diagnosis problem into the joint estimation of LIB states and ISC resistance. Two primary contributions are made.

First, a theoretically-proven ISC diagnostic method is proposed by discounting the capacity dependence. The model switching architecture guarantees a compromise of the steady-state accuracy and start-up convergence, which can be tough due to the co-estimation of cross-interfaced variables. Second, the recursive total least squares method with variant forgetting (RTLS-VF) is proposed to compensate for the effect of noise-corruptive data acquisition. This virtually contributes to a noise-immune and unbiased estimate of the ISC resistance.

This work is the first one we are aware of that scrutinizes the impact of aging and disturbances to ISC diagnostic as well as the associated methods for overcoming such adverse effect, with a potential for transforming its practical use in real-time embedded battery management systems.

The remainder of this paper is organized as follows. The model-based ISC diagnostic is detailed in section II. The RTLS-VF for ISC resistance estimate is elaborated in Section III. Simulation and experimental results are discussed in Section IV and V. Primary conclusions are drawn in Section VI.

II. Model-Based ISC Diagnostic

A. Modelling

A battery model with high fidelity yet sufficient simplicity underlies the model-based diagnosis methods. As shown in Fig. 1 (a), the used first-order normal cell model consists the SOC-dependent OCV, ohmic resistance (R_0), and a RC branch simulating the polarization effects. Such impedance parameters can be calibrated easily with the pulse-relaxation method.

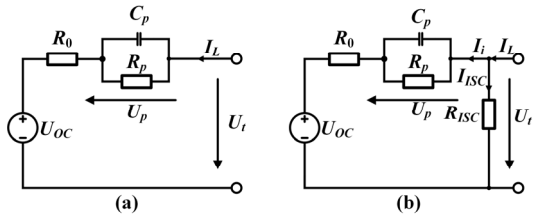

Fig. 1 ECMs: (a) normal cell model, and (b) faulty cell model with ISC.

The dynamics of normal cell model is described by:

$$C_p \frac{dU_p(t)}{dt} = I_L(t) - \frac{U_p(t)}{R_p} \tag{1.a}$$

$$U_t(t) = U_{OC}(t) + I_L(t) R_0 + U_p(t) \tag{1.b}$$

$$\frac{dz(t)}{dt} = \frac{\eta I_L(t)}{Q_0} \tag{1.c}$$

where t is the time, I_L the load current, z the SOC, η the coulombic efficiency, Q_0 the nominal capacity, U_p and U_t respectively the polarization and terminal voltage, and U_{OC} the OCV expressed as a function of battery SOC:

$$U_{OC} = f(z) = \sum_{i=0}^{n} c_i z^i \tag{2}$$

where n is the polynomial order, c_i is the polynomial coefficient determined by polynomial fitting the SOC-OCV testing data. The extracted coefficients of SOC-OCV function are summarized in Table I.

TABLE I
POLYNOMIAL COEFFICIENTS OF SOC-OCV FUNCTION

Coefficients	c_0	c_1	c_2	c_3	c_4
Value	3.301	2.176	-6.353	8.839	-3.805

On this premise, the ISC cell can be modeled electrically by adding a current by-pass with a specific ISC resistance, as shown in Fig. 1 (b), where I_i is the electrochemical current, I_{ISC} is the current passing the ISC resistance. The dynamics of faulty cell is derived by replacing I_L in (1) with $I_i = I_L - U_t / R_{ISC}$:

$$C_p \frac{dU_p(t)}{dt} = I_L(t) - \frac{U_t(t)}{R_{ISC}} - \frac{U_p(t)}{R_p} \tag{3.a}$$

$$U_t(t) = \frac{R_{ISC}}{R_0 + R_{ISC}} \left(U_{OC}(t) + I_L(t) R_0 + U_p(t) \right) \tag{3.b}$$

$$\frac{dz(t)}{dt} = \frac{\eta I_L(t)}{Q_0} - \frac{\eta U_t(t)}{R_{ISC} Q_0} \tag{3.c}$$

B. Multi-state-fusion ISC Diagnostic

Commonly-used ISC diagnostic methods based on abnormal charge depletion are sensitive to the capacity fading of LIB. To remedy this deficiency, a multi-state-fusion ISC diagnostic method is proposed without using the capacity to enhance the robustness to battery degradation.

As can be seen in Fig. 1 (b), assuming that U_{OC} and U_p are already known or estimated accurately, the unmeasurable electrochemical current can be derived by:

$$I_i(k)=\frac{U_t(k)-U_{OC}(k)-U_p(k)}{R_0} \tag{4}$$

The ISC current is hence given by:

$$I_{ISC}(k)=I_L(k)-I_i(k) \tag{5}$$

The quantitative diagnostic of ISC severity boils down to determining the exact value of the ISC resistance. To this end, a regression problem can be formulated by:

$$h(k)=R_{ISC}\varphi(k) \tag{6}$$

where $h(k) = U_t(k)$, $\varphi(k) = I_{ISC}(k)$.

It is explicit that the ISC resistant can be identified by solving the regression model (6). This can be achieved by a broad variety of optimization methods like the most commonly-used least squares (LS) algorithm. However, the measurement noises on current and voltage as well as the numerical error give rise to a large risk of biased identification. This will be a major endeavor of this work, and will left for detailing in Section III.

Referring to (4)-(6), it is evident that U_t can be measured directly, and U_{OC} is SOC-dependent. Therefore, a state observer is formulated to estimate SOC and U_p. The state of interest, input and output are defined as: $\boldsymbol{x}(k) = [U_p(k)\ z(k)]^{\boldsymbol{T}}$, $\boldsymbol{u}(k) = [I_L(k)\ U_t(k)]^{\boldsymbol{T}}$, $y(k) = U_t(k)$. Referring to the faulty cell model (3), The discrete-time state-space model can be expressed as:

$$\begin{aligned}\boldsymbol{x}(k+1)&=\boldsymbol{A}\boldsymbol{x}(k)+\boldsymbol{B}(k)\boldsymbol{u}(k)+\boldsymbol{w}(k)\\ y(k)&=\boldsymbol{F}(\boldsymbol{x}(k),\boldsymbol{u}(k))+v(k)\end{aligned} \tag{7}$$

where

$$\boldsymbol{A}=\begin{bmatrix} e^{-\frac{\Delta t}{R_pC_p}} & 0\\ 0 & 1\end{bmatrix},\boldsymbol{B}(k)=\begin{bmatrix}\left(1-e^{-\frac{\Delta t}{R_pC_p}}\right)R_p & \frac{\left(e^{-\frac{\Delta t}{R_pC_p}}-1\right)R_p}{R_{ISC}(k-1)}\\ \frac{\Delta t}{Q_0} & \frac{-\Delta t}{R_{ISC}(k-1)Q_0}\end{bmatrix}^{\boldsymbol{T}}$$

$$\boldsymbol{F}(\boldsymbol{x}(k),\boldsymbol{u}(k))=\xi\left(U_p(k)+f(z(k))+R_0I_L(k)\right)$$

where $\xi = R_{ISC}(k-1)/(R_{ISC}(k-1)+R_0)$, Δt is the time interval, $\boldsymbol{w}(k)$ is the process noise with covariance matrix $\boldsymbol{\Sigma_w}$, while $v(k)$ is the measurement noise of $y(k)$ with covariance matrix Σ_v.

C. Model Switching Framework

Noted that the R_{ISC} is estimated at each iteration and, in return feedback to the faulty cell model, to ensure the accuracy of the battery modeling and state estimation. However, the concurrent estimation of R_{ISC}, SOC, and U_p can incur remarkable cross interference which may impair the convergence. In this regard, a model switching framework is built by incorporating a normal cell model and a faulty cell model to improve the convergence property while keep a high steady-state diagnostic accuracy. Specifically, the normal cell model is used at the beginning of the diagnostic. Once the accumulated ampere-hour throughput exceeds a certain threshold assuring the convergence of R_{ISC} estimations, the faulty cell model with the estimated R_{ISC} is used to improve the accuracy of the state estimation. The faulty cell model will be updated at the beginning of each iteration with the estimations at previous iteration.

With respect to the normal cell state observation, the state, input and output are defined alternatively by: $\boldsymbol{x_1}(k) = [U_p(k)\ z(k)]^{\boldsymbol{T}}$, $u_1(k) = I_L(k)$, $y_1(k) = U_t(k)$. With the built normal cell model, the state-space expression is given by:

$$\begin{aligned}\boldsymbol{x}_1(k+1)&=\boldsymbol{A}_1\boldsymbol{x}_1(k)+\boldsymbol{B}_1(k)u_1(k)+\boldsymbol{w}(k)\\ y_1(k)&=F_1(\boldsymbol{x}_1(k),u_1(k))+v(k)\end{aligned} \tag{8}$$

where

$$\boldsymbol{A}_1=\begin{bmatrix} e^{-\frac{\Delta t}{R_pC_p}} & 0\\ 0 & 1\end{bmatrix},\boldsymbol{B}_1(k)=\begin{bmatrix}\left(1-e^{-\frac{\Delta t}{R_pC_p}}\right)R_p & \frac{\Delta t}{Q_0}\end{bmatrix}^{\boldsymbol{T}},$$

$$F_1(\boldsymbol{x}_1(k),u_1(k))=f(z(k))+U_p(k)+R_0u_1(k)$$

With the established discrete-time state-space model, SOC and U_p are estimated using the EKF in this paper.

D. Theoretical proof of aging robustness

The multi-state-fusion framework is expected to mitigate the capacity deviation-induced uncertainty. A theoretical proof of this is presented herein. We make a practical assumption that the capacity drops from the nominal Q_0 to Q_r during the aging, while the method is unaware of this. At a given time step, the priori update of SOC and error covariance are given by:

$$\begin{aligned}\hat{z}_k^-&=\hat{z}_{k-1}+I_{L,k-1}\Delta t/Q_0\\ \hat{P}_k^-&=\hat{P}_{k-1}+Q\end{aligned} \tag{9}$$

where $\hat{P}$ is the SOC error variance, Q is the process noise variance, and the superscript $^-$ denotes the priori update. The posteriori SOC estimate is updated via the error feedback:

$$\hat{z}_k=\hat{z}_k^-+L_k\left(V_{t,k}-\hat{V}_{t,k}^-\right) \tag{10}$$

The Kalman gain L_k in (30) is calculated as:

$$L_k=\hat{P}_k^-\hat{\tau}_k^T\left(\hat{\tau}_k\hat{P}_k^-\hat{\tau}_k^T+R\right)^{-1} \tag{11}$$

where R is the measurement noise variance. Meanwhile, $\hat{P}$ is updated as

$$\hat{P}_k=\left(1-L_k\hat{\tau}_k\right)\hat{P}_k^- \tag{12}$$

In (11) and (12), $\hat{\tau}_k$ is the derivative of U_{OC} with respect to $\hat{z}_k^-$, i.e.,

$$\hat{\tau}_k=\left.\frac{df(z)}{dz}\right|_{\hat{z}_k^-} \tag{13}$$

The recursive expression of z_k can be obtained by combining (9) and (10) as:

$$\hat{z}_k^-=\hat{z}_{k-1}+\frac{I_{L,k-1}\Delta t}{Q_0}+L_k\left(V_{t,k}-\hat{V}_{t,k}^-\right) \tag{14}$$

where

$$\begin{aligned}V_{t,k}&=f\left(z_k^*\right)+V_{p,k}^*+I_{L,k}R_0\\ \hat{V}_{t,k}^-&=f\left(\hat{z}_k^-\right)+\hat{V}_{p,k}+I_{L,k}R_0\end{aligned} \tag{15}$$

where the superscript * denotes the true value.

It is explicit from (7-8) that the polarization voltage is not affected by the capacity error, so that $\hat{V}_{p,k} = V^*_{p,k}$, and the voltage error is given by:

$$V_{t,k} - \hat{V}^-_{t,k} = f\left(z^*_k\right) - f\left(\hat{z}^-_k\right) \tag{16}$$

The following approximation holds as $\hat{z}_k$ is typically not too far away from z^*_k [31]:

$$\begin{aligned} f\left(z^*_k\right) - f\left(\hat{z}^-_k\right) &= f\left(z^*_{k-1} + \frac{I_{L,k-1}\Delta t}{Q_r}\right) - f\left(\hat{z}^-_{k-1} + \frac{I_{L,k-1}\Delta t}{Q_0}\right) \\ &\approx f\left(z^*_{k-1}\right) + \tau_k \frac{I_{L,k-1}\Delta t}{Q_r} - f\left(\hat{z}^-_{k-1}\right) - \tau_k \frac{I_{L,k-1}\Delta t}{Q_0} \\ &\approx \tau_k \Delta z_{k-1} + \tau_k I_{L,k-1}\Delta t\left(\frac{1}{Q_r} - \frac{1}{Q_0}\right) \end{aligned} \tag{17}$$

Then the SOC estimate can be derived by substituting (17) into (14):

$$\hat{z}_k = \hat{z}^-_k + L_k\left(\tau_k \Delta z_{k-1} + \tau_k I_{L,k-1}\Delta t\left(1/Q_r - 1/Q_0\right)\right) \tag{18}$$

whilst the true SOC is given by:

$$z^*_k = z^*_{k-1} + I_{L,k-1}\Delta t / C_r \tag{19}$$

By subtracting (18) from (19), the recursive expression of the estimation error ($\Delta z_k = z_k^* - \hat{z}_k$) can be obtained as:

$$\Delta z_k = \left(1 - \tau_k L_k\right)\Delta z_{k-1} + \left(1 - \tau_k L_k\right) I_{L,k-1}\Delta t\left(1/Q_r - 1/Q_0\right) \tag{20}$$

With an SOC guess error Δz_0, the solution of Δz_k is:

$$\begin{aligned} \Delta z_k &= \prod_{i=1}^{k}\left(1 - \tau_i L_i\right)\Delta z_0 \\ &+ \sum_{i=1}^{k}\left(\prod_{m=i}^{k}\left(1 - \tau_m L_m\right) I_{L,i-1}\Delta t\left(1/Q_r - 1/Q_0\right)\right) \end{aligned} \tag{21}$$

Noted that the OCV is piece-wise linear for typical LIBs. The OCV slope of the NMC battery is close to a constant $\tau = 0.65$ mV/1% SOC within the operating range of 10–100 % SOC [31]. In this case, it is proved that the feedback gain L converges to the range of $0 < L < 1/\tau$. L is very closed to $1/\tau$ if R is small enough. Therefore, as $k \to \infty$, the estimation error is:

$$\left(\frac{1}{\tau L} - 1\right) I_{L,\min}\Delta t\left(\frac{Q_0 - Q_r}{Q_r Q_0}\right) < \Delta z_k < \left(\frac{1}{\tau L} - 1\right) I_{L,\max}\Delta t\left(\frac{Q_0 - Q_r}{Q_r Q_0}\right) \tag{22}$$

Thus, the absolute estimation error of SOC is given by:

$$\left|\Delta z_k\right| < \frac{4}{Q_r}\left(\frac{1}{\tau L} - 1\right)\left(\frac{Q_0 - Q_r}{Q_0}\right) \tag{23}$$

The true value and the estimates of I_{ISC} can be expressed via (5) and (6) as:

$$\begin{aligned} I^*_{ISC,k} &= I_{L,k} - \left(U_{t,k} - U^*_{OC,k} - U^*_{p,k}\right)/R_0 \\ \hat{I}_{ISC,k} &= I_{L,k} - \left(U_{t,k} - \hat{U}_{OC,k} - \hat{U}_{p,k}\right)/R_0 \end{aligned} \tag{24}$$

Hence, the R_{ISC} estimation error can be obtained as:

$$\begin{aligned} \Delta R_{ISC,k} &= U_{t,k}/I^*_{ISC,k} - U_{t,k}/\hat{I}_{ISC,k} \\ &= U_{t,k}\left(\frac{\hat{I}_{ISC,k} - I^*_{ISC,k}}{I^*_{ISC,k}\hat{I}_{ISC,k}}\right) = \frac{U_{t,k}\tau\Delta z_k}{R_0 I^*_{ISC,k}\hat{I}_{ISC,k}} \end{aligned} \tag{25}$$

By substituting (23) into (25), the relationship between the R_{ISC} estimation error and the capacity error can be expressed as:

$$\left|\Delta R_{ISC,k}\right| < \frac{4U_{t,k}\left(1/L - \tau\right)}{Q_r R_0 I^*_{ISC,k}\hat{I}_{ISC,k}}\frac{\left(Q_0 - Q_r\right)}{Q_0} \tag{26}$$

Recall that the feedback gain L converges to the range of $0 < L < 1/\tau$, and L approximates to $1/\tau$ if R is tuned to be sufficiently small. Hence, it is validated that the R_{ISC} estimation error theoretically converges to 0 via effective EKF tuning. This completes the proof of aging robustness.

III. Disturbance-Immune ISC Resistance Estimation

The quantitative diagnostic of ISC needs an accurate solution of (6). The widely-used LS is proved to be biased due to the noise corruption in this section. A RTLS-VF-based noise-immune method is elaborated to mitigate the noise effect.

A. Error-in-Variables Analysis

The LS assumes that noises corrupt only the system output, which is not necessarily in accordance with the reality as the input $I_{ISC}(k)$ is also subject to disturbances due to the estimation error and noises on current measurement. With the presence of noises, the input and output observation of (6) are:

$$\tilde{\varphi}(k) = \varphi(k) + \Delta\varphi(k), \tilde{h}(k) = h(k) + \Delta h(k) \tag{27}$$

where $\Delta h(k)$ and $\Delta\varphi(k)$ are the disturbances on $h(k)$ and $\varphi(k)$, respectively. Both Δh and $\Delta\varphi$ are assumed to be zero mean, normally distributed random variables with variances of δ_u^2 and δ_i^2, respectively. The noise corruption recasts (6) a typical error-in-variable (EIV) system which challenges the suitability of LS method for an unbiased solution.

Definition*:** The auto- and cross-covariance matrices of two arbitrary vectors (m*** and ***n***) are defined by (28.a), and the auto- and cross-covariance functions of two arbitrary scalar stochastic processes (r and d) are defined by (29.b).

$$\boldsymbol{\Sigma_m} = E\left[\boldsymbol{m}\boldsymbol{m}^{\boldsymbol{T}}\right], \boldsymbol{\Sigma_{mn}} = E\left[\boldsymbol{m}\boldsymbol{n}^{\boldsymbol{T}}\right] \tag{28.a}$$

$$\Sigma_r = E\left[rr\right], \qquad \Sigma_{rd} = E\left[rd\right] \tag{29.b}$$

where $E[\bullet]$ is the expected value operator.

The well-known LS solution of (6) is given by:

$$R^{LS}_{ISC} = \Sigma^{-1}_{\tilde{\varphi}}\Sigma_{\tilde{\varphi}\tilde{h}} = \left(\Sigma_{\varphi} + \Sigma_{\Delta\varphi}\right)^{-1}\left(\Sigma_{\varphi h} + \Sigma_{\Delta\varphi h}\right) \tag{30}$$

With the participation of noises, instead, the compensated unbiased solution is given by:

$$R^*_{ISC} = \Sigma^{-1}_{\varphi}\Sigma_{\varphi h} = \left(\Sigma_{\tilde{\varphi}} - \Sigma_{\Delta\varphi}\right)^{-1}\left(\Sigma_{\tilde{\varphi}\tilde{h}} - \Sigma_{\Delta\varphi\Delta h}\right) \tag{31}$$

Being aware that $\Sigma_{\Delta\varphi\Delta y} = 0$, and applying the matrix inversion lemma to (30) yields:

$$R^{LS}_{ISC} = \left[\Sigma^{-1}_{\varphi} - \Sigma^{-1}_{\varphi}\left(\Sigma^{-1}_{\varphi} + \Sigma^{-1}_{\Delta\varphi}\right)^{-1}\Sigma^{-1}_{\varphi}\right]\Sigma_{\varphi h} \tag{32}$$

Combining (31) and (32), the LS bias is finalized by:

$$R^{bias}_{ISC} = -\Sigma^{-1}_{\varphi}\left(\Sigma^{-1}_{\varphi} + \Sigma^{-1}_{\Delta\varphi}\right)^{-1} R^*_{ISC} \tag{33}$$

Herein the LS validates to be asymptotically biased once both the system input and output are disturbed with noises.

B. TLS Fundamental

Unlike the LS to minimize the Euclidean norm of estimation error vector, the total least squares (TLS) algorithm minimizes simultaneously the perturbations on system input and output so that the unbiased regressive solution can be found [32, 33]. In accordance with this, (6) is transformed to:

$$\underbrace{h(k)+\Delta h(k)}_{\tilde{h}(k)} = R_{ISC}\underbrace{\left(\varphi(k)+\Delta\varphi(k)\right)}_{\tilde{\varphi}(k)} \tag{34}$$

In particular, the TLS is solved by finding the minimum perturbation matrices i.e., $\Delta\boldsymbol{H}(k)$ and $\Delta\boldsymbol{\Psi}(k)$, and the R_{ISC} estimate that satisfy:

$$\tilde{\boldsymbol{h}}(k)+\Delta\boldsymbol{H}(k)=\hat{R}_{ISC}(k)\left(\tilde{\boldsymbol{\varphi}}(k)+\Delta\boldsymbol{\Psi}(k)\right) \tag{35}$$

where

$$\tilde{\boldsymbol{h}}(k)=\left[\tilde{h}(k),\tilde{h}(k-1),...,\tilde{h}(1)\right]$$
$$\tilde{\boldsymbol{\varphi}}(k)=\left[\tilde{\varphi}(k),\tilde{\varphi}(k-1),...,\tilde{\varphi}(1)\right]$$

If the unit weighting is used, the TLS boils down to solve the following minimization problem:

$$\hat{R}_{ISC}=\arg\min_{\hat{R}_{ISC},\Delta\boldsymbol{\Psi},\Delta\boldsymbol{H}}\left\|\Delta\boldsymbol{\Psi}(k)\middle|\Delta\boldsymbol{H}(k)\right\|_F \tag{36}$$

where $\|\cdot\|_F$ denotes the Frobenius norm.

Define $\boldsymbol{q}=[R_{ISC}, -1]^T$, then $R_{ISC}(k)$ is equal to the TLS estimate provided that $\boldsymbol{q}_k$ is the eigenvector corresponding to the smallest eigenvalue of the following covariance matrix [34]:

$$\boldsymbol{\Sigma}_{\bar{\varphi}}(k)=E\left[\bar{\boldsymbol{\varphi}}(k)\bar{\boldsymbol{\varphi}}^T(k)\right]=\begin{bmatrix}\Sigma_{\tilde{\varphi}}(k) & \Sigma_{\tilde{\varphi}\tilde{h}}(k)\\ \Sigma_{\tilde{h}\tilde{\varphi}}(k) & \Sigma_{\tilde{h}}(k)\end{bmatrix} \tag{37}$$

where $\bar{\boldsymbol{\varphi}}(k)=\begin{bmatrix}\tilde{\varphi}(k) & \tilde{h}(k)\end{bmatrix}^T$.

The least eigenvalue problem can be solved by the singular value decomposition (SVD), but its cubic complexity discounts the potential for online application. It is hence desired to find an efficient recursive version of the TLS, in seeking to ease its application in the low-cost embedded system.

C. Numerical Solution of TLS

Theorem 1: The solution given by (38) is a TLS solution to the EIV problem defined by (6). This solution is asymptotically unbiased even if the system inputs and outputs are both corrupted by noises.

$$\boldsymbol{q}=\arg\min_{\boldsymbol{q}} g\left(\boldsymbol{\Sigma}_{\bar{\varphi}},\boldsymbol{q}\right)$$
$$\text{with } g\left(\boldsymbol{\Sigma}_{\bar{\varphi}},\boldsymbol{q}\right)=\boldsymbol{q}^T\boldsymbol{\Sigma}_{\bar{\varphi}}\boldsymbol{q}\Big/\left(\boldsymbol{q}^T\boldsymbol{D}\boldsymbol{q}\right) \tag{38}$$

where $\boldsymbol{D}=diag\,(1, \beta^{-1/2})$ with $\beta=\delta_u^2/\delta_i^2$.

Proof: Equation (38) is realized if:

$$\partial g\left(\boldsymbol{\Sigma}_{\bar{\varphi}}(k),\boldsymbol{q}(k)\right)\Big/\partial\boldsymbol{q}(k)=0$$

which can be further transferred to the following equality that the TLS solution follows:

$$\boldsymbol{\Sigma}_{\bar{\varphi}}(k)\boldsymbol{q}(k)=\rho\boldsymbol{D}\boldsymbol{q}(k) \tag{39}$$

where $\rho=g\left(\boldsymbol{\Sigma}_{\bar{\varphi}}(k),\boldsymbol{q}(k)\right)$. It is hence validated that the given solution complies to the TLS requirement. Moreover, (39) can be expressed alternatively as:

$$\left\{\begin{bmatrix}\Sigma_{\tilde{\varphi}} & \Sigma_{\tilde{\varphi}\tilde{h}}\\ \Sigma_{\tilde{h}\tilde{\varphi}} & \Sigma_{\tilde{h}}\end{bmatrix}+\begin{bmatrix}\delta_i^2 & 0\\ 0 & \delta_u^2\end{bmatrix}\right\}\begin{bmatrix}R_{ISC}^{TLS}\\ -1\end{bmatrix}=\rho\boldsymbol{D}\begin{bmatrix}R_{ISC}^{TLS}\\ -1\end{bmatrix} \tag{40}$$

Assume the solution is equal to the unbiased estimate of R_{ISC}, i.e., $R_{ISC}^{TLS}=R_{ISC}^{*}=\Sigma_{\varphi}^{-1}\Sigma_{\varphi h}$, substituting this to (40) confirms the equality with $\rho=\delta_i^2$. In other words, $\left[R_{ISC}^{TLS}, -1\right]^T$ is a generalized eigenvector with corresponding eigenvalue $\Lambda_{\min}=\delta_i^2$. The asymptotic unbiased feature of R_{ISC}^{TLS} is hence validated.

Recall that $\boldsymbol{q}=[R_{ISC}, -1]^T$, (38) can be rewritten as:

$$g\left(\boldsymbol{\Sigma}_{\bar{\varphi}},R_{ISC}\right)=\frac{\left[R_{ISC},-1\right]\boldsymbol{\Sigma}_{\bar{\varphi}}\left[R_{ISC},-1\right]^T}{\left[R_{ISC},-1\right]\boldsymbol{D}\left[R_{ISC},-1\right]^T}$$
$$=\left(\Sigma_{\tilde{\varphi}}R_{ISC}^2-2\boldsymbol{\Sigma}_{\tilde{\varphi}\tilde{h}}R_{ISC}+\boldsymbol{\Sigma}_{\tilde{h}}\right)\Big/\left(R_{ISC}^2+\beta\right) \tag{41}$$

The minimization problem (41) is solved using the gradient search method in this paper. Particularly, R_{ISC} is updated by:

$$\hat{R}_{ISC}(k)=\hat{R}_{ISC}(k-1)+\alpha(k)\tilde{\varphi}(k) \tag{42}$$

where $\alpha(k)$ is an adaptive gain which can be calculated by:

$$\partial g\left(\boldsymbol{\Sigma}_{\bar{\varphi}}(k),R_{ISC}(k)\right)\Big/\partial\alpha(k)=0 \tag{43}$$

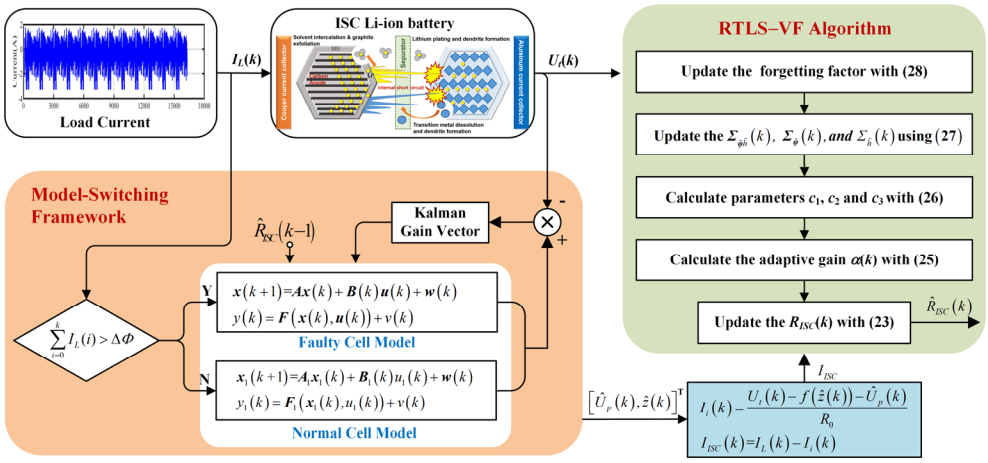

Fig. 2 Scheme of the proposed ISC diagnostic method.

Combining (41)-(43) gives the following quadratic equation which can be easily solved:

$$c_1\alpha^2(k)+c_2\alpha(k)+c_3=0 \tag{44}$$

where

$$\begin{aligned} c_1 &= 2\tilde{\varphi}(k)^3\,\Sigma_{\tilde{\varphi}\tilde{h}}(k) \\ c_2 &= 2\tilde{\varphi}(k)^2\left(2\Sigma_{\tilde{\varphi}\tilde{h}}(k)\hat{R}_{ISC}(k-1)+\beta\Sigma_{\tilde{\varphi}}(k)-\Sigma_{\tilde{h}}(k)\right) \\ c_3 &= 2\tilde{\varphi}(k)\begin{pmatrix}\Sigma_{\tilde{\varphi}\tilde{h}}\hat{R}_{ISC}^2(k-1)+\beta\Sigma_{\tilde{\varphi}\tilde{h}}(k)\\ -\left(\beta\Sigma_{\tilde{\varphi}}(k)+\Sigma_{\tilde{h}}(k)\right)\hat{R}_{ISC}(k-1)\end{pmatrix} \end{aligned} \tag{45}$$

The covariance terms in (45) are updated recursively, giving rise to an efficient recursive TLS (RTLS) method. A general propagation law applicable to all terms is given by:

$$\begin{aligned} \boldsymbol{\Sigma}_{\boldsymbol{mn}}(k+1) &= (1-\gamma_k)\boldsymbol{\Sigma}_{\boldsymbol{mn}}(k)+\gamma_k\boldsymbol{m}(k)\boldsymbol{n}^T(k) \\ \gamma_k &\triangleq \left(1+\sum_{i=1}^{k-1}\prod_{j=i+1}^{k}\lambda_j\right)^{-1}=\gamma_{k-1}/(\lambda_k+\gamma_{k-1}) \end{aligned} \tag{46}$$

where λ is the forgetting factor ($0.95<\lambda<1$). It is worth noting that λ is tied to the conflicting objective of tracking alertness and stability [35]. A variant forgetting (VF) rule is used herein:

$$\lambda(k)=\lambda_{\min}+(1-\lambda_{\min})\cdot 2^{-2\varepsilon^2(k)} \tag{47}$$

where $\varepsilon(k)=\tilde{h}(k)-\hat{R}_{ISC}(k)\tilde{\varphi}(k)$. The overall framework of the proposed ISC diagnostic method is shown in Fig. 2.

IV. Simulation Results

Simulations are carried out to evaluate different methods in this section. The use of ideal battery model ensures that the methods are evaluated from the theoretical prospective without the disturbances from model uncertainties.

A. Data Acquisition

The faulty cell model as shown in Fig. 1 (b) was built to simulate a cell with ISC fault. With the available knowledge on the LIB in use, R_0, R_p, C_p, and Q_r are defined as constants of 50 mΩ, 20 mΩ, 1000 F, and 2.2 Ah, respectively. The federal urban driving schedule (FUDS) current profile was loaded to excite the battery model. The current, voltage and reference SOC are sampled at 1 Hz. The current sensor in industrial processes contains errors within the range of 0.1% ~ 1% [36]. In contrast, commercial voltage management circuits for LIB have a high accuracy with the error confined to less than 2 mV. Even for the application in practical environment, most of the voltage sensors can suppress the error to 5 mV [37], or even as low as 1 ~ 2 mV [36]. Hence, random noises with standard deviations of 10 mA and 4 mV are added herein to the noise-free current and voltage signals to simulate a typical noise-corrupted condition.

The equivalent resistance (ER) approach with external short circuit to represent ISC shows the merit of high controllability [38]. To this end, the ISC resistance needs to be selected properly to simulate a practical early-stage ISC fault. The electro-thermal prosperities of ISC were analyzed utilizing ERs from 10 Ω to 100 Ω in [18]. It is found that with R_{ISC} > 20 Ω, the voltage and the temperature responses hardly show any abnormity, indicating that the direct ISC detection using voltage and temperature is difficult. With an ISC resistance of 10 Ω, the LIB temperature builds up to the safety threshold beyond which the self-heating will be triggered. Hence, the early-stage ISC diagnostic (R_{ISC} > 10 Ω) is essential. In this paper, a 25 Ω ER is used to represent an early-stage ISC with unobservable voltage and temperature abnormity, while a 10 Ω ER is used to represent an ISC fault approaching the threshold of severe thermal consequences. This also draws a direct link from the ISC resistance estimation to the ISC severity diagnostic.

B. Simulation Results with Constant ISC Resistance

The capacity is assumed to 11% biased from the ground truth to verify the robustness of proposed method to capacity fade. The estimates of SOC, I_{ISC}, and R_{ISC} are plotted in Fig. 3, while the mean absolute error (MAE) and rooted mean square error (RMSE) of estimation are tabulated in Table II. As can be seen in Fig. 3 (a) and (d), the SOC estimates for both cases converge from the initialization error and track the reference SOC trajectories closely. The capacity error shows no obvious impact on the SOC estimate, suggested by the minimal estimation error observed. This is explained by the voltage error-based correction which mitigates effectively the capacity deviation-induced state mismatch. By comparison, the I_{ISC} estimates shown in Fig. 3 (b) and (e) vibrate heavily around the benchmarks. This is a two-fold consequence contributed by both the disturbances on input current and the uncertainties of estimated states, referring to (4)-(5).

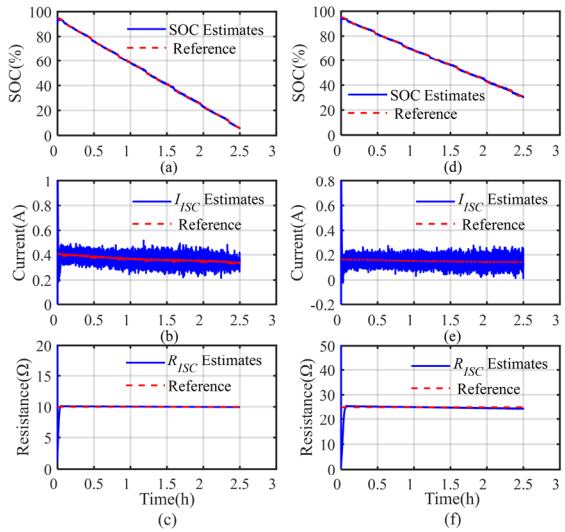

Fig. 3 Estimation results of SOC, I_{ISC}, and R_{ISC} of 10 Ω R_{ISC} case and 25Ω R_{ISC} case: (a) SOC estimates of 10 Ω R_{ISC}, (b) I_{ISC} estimates of 10 Ω R_{ISC}, (c) R_{ISC} estimates of 10 Ω R_{ISC}, (d) SOC estimates of 25 Ω R_{ISC}, (e) I_{ISC} estimates of 25 Ω R_{ISC}, (f) R_{ISC} estimates of 25 Ω R_{ISC}

TABLE II
ESTIMATION ERROR OF SOC AND ISC RESISTANCE

	MAE	RMSE
SOC-10 Ω	0.1213 %	0.2004 %
R_{ISC}-10Ω	0.3094 Ω	0.3296 Ω
SOC-25 Ω	0.1189 %	0.1901 %
R_{ISC}-25Ω	0.4934 Ω	0.6082 Ω

Despite the noisy I_{ISC} estimates, it can be seen in Fig. 3 (c) and (f) that the R_{ISC} estimates converge to the reference value stably and precisely. This is because the presented EIV problem can be well solved by the RTLS algorithm, which is a major contribution of the proposed method. Again, the capacity deviation has no observable impact to the R_{ISC} estimation, which is attributed to the capacity independence of the multi-state-fusion framework. The accurate estimation of R_{ISC} with different values directly validates the capability of the proposed method in diagnosing ISC faults with different severities.

C. Simulation Results with Changed ISC Resistance

This section goes further to validate the effectiveness of the proposed method under a sudden change of the R_{ISC}. For this purpose, the ISC resistance is defined to drop instantaneously from 25 Ω to 10 Ω at the halfway of simulation. The estimates of SOC, I_{ISC}, and R_{ISC} of this study are plotted in Fig. 4. As shown, the SOC estimates converge to and resemble the benchmarked values accurately regardless of the sudden change of ISC resistance. The MAE and RMSE of SOC estimation are as low as 0.142 % and 0.212 %. More pronouncedly, the proposed method succeeds to track the sudden change of ISC current/resistance with a rapid convergence and close steady-state agreement. Although the I_{ISC} estimates contain high-frequency errors due to the disturbances and state uncertainties, the R_{ISC} is highly authentic and much more stable. The statistical result suggests that the MAE and RMSE of R_{ISC} estimation are only 1.298 Ω and 2.180 Ω, respectively.

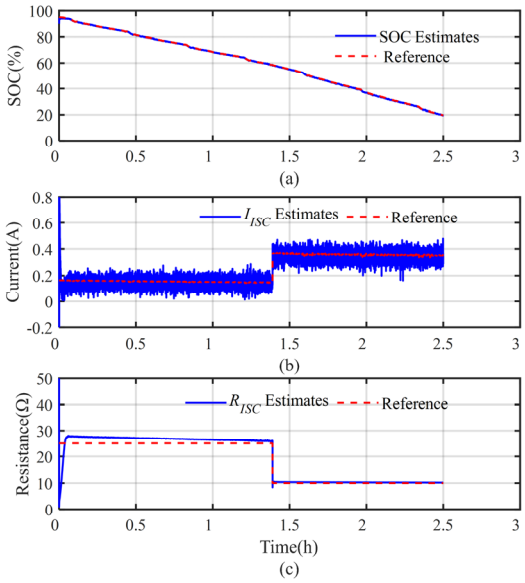

Fig. 4 Estimation results of SOC, I_{ISC}, and R_{ISC} under a sudden change of ISC resistance: (a) SOC, (b) I_{ISC}, (c) R_{ISC}.

V. Experimental Results

A. Experiment Details

Experiments are carried on a 18650 NMC battery. The cell was enclosed in a Vötsch thermal chamber to keep a constant ambient temperature of 25 °C. The FUDS current profile was applied on the cell via the Arbin battery testing system, where the current and voltage were sampled precisely with error limits less than 0.05%. The ER approach is used to validate the early-stage ISC diagnostic. For real-time performance evaluation, Freescale's MPC5554 was employed as an embedded micro-controller unit (MCU). The proposed method was compiled into the machine code and written into the MCU, while the CAN bus was used to transmit the load current and terminal voltage measurements. The SOC estimation and ISC diagnostic were executed with the target MCU in real time at a time interval of 1 second.

To validate the SOC estimation, CC-CV charging is applied to fully charge the cell, and then CC discharge is applied to pre-set the cell at a known SOC. Being aware of the initial SOC, the benchmarked SOC during the subsequent experiment can be obtained leveraging the coulomb counting (CC) method. The current and terminal voltage measurements, as well as the reference SOCs are plotted in Fig. 5. The reference ISC current can be calculated directly by dividing the terminal voltage by the value of ER to assess the accuracy of ISC current estimation.

To validate the robustness against capacity fading, validation experiments are performed on an aged cell (SOH = 89.0%), while the capacity of fresh cell is intentionally used for the proposed method throughout this paper. The model parameters in the experimental study were identified offline at different battery SOCs. The SOC-dependency of parameters, as shown in Fig. 6, was determined using the look-up table. The ECM parameter extraction has been studied widely [25-30], thus is not detailed herein. The impedance parameters are imposed with 20 % error to generate a high model uncertainty.

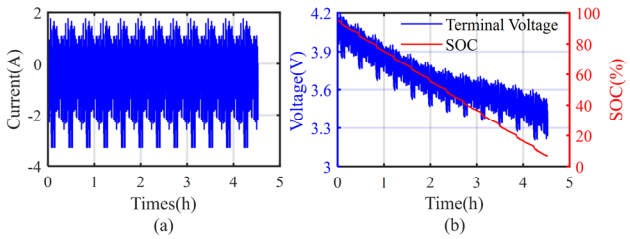

Fig. 5 FUDS: (a) current, and (b) terminal voltage and SOC

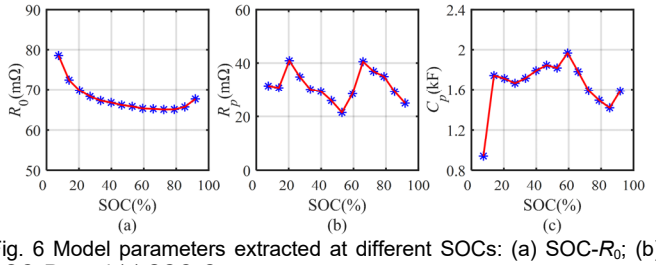

Fig. 6 Model parameters extracted at different SOCs: (a) SOC-R_0; (b) SOC-R_p; and (c) SOC-C_p

Throughout the validation, the proposed method is compared with two reference methods for more reasonable evaluation. Noted that the parameter selection and initialization condition are consistent for all the three methods for a fair comparison.

Method 1, named as "SOC-based", represents the state-of-the-art progress in the literature. Referring to Fig. 1 (b), the ISC

resistance gives the faulty cell an extra path for current bypass. This bypassing current causes an abnormal charge depletion, which is used as a clue to estimate the R_{ISC}. First, the SOC is estimated by using EKF for a fair comparison, and then the electrochemical current is given by:

$$I_i(k) = \left(z(k) - z(k-1)\right)Q_0 \tag{48}$$

Therefore, the ISC current is calculated by the mismatch between the electrochemical current and load current:

$$I_{ISC}(k) = I_L(k) - \left(z(k) - z(k-1)\right)Q_0 \tag{49}$$

The formulated regression problem is solved by using the RTLS-VF method. This idea has been widely used for the ISC diagnostic of both single-cell [19, 21] and LIB pack [16, 17].

Method 2, named as "NCM-MS", is the counterpart of the proposed method by replacing the switching model structure with the normal cell model. The comparison with this method further validates the necessity of model switching.

B. Validation of State Estimation and ISC Diagnostic

The model switching framework is expected to improve the convergence property and steady-state accuracy. A direct justification of this can be made by comparing the proposed method with the NCM-MS method, as shown in Fig. 7. The corresponding MAE and RMSE of estimation are summarized in Table III. It is shown that with a large R_{ISC} of 25 Ω, both the two methods converge from the initialization error and resemble the reference SOC trajectories closely. This is because a larger R_{ISC} means an earlier stage of ISC where the leakage current is commonly ignorable to cause a model mismatch. As the R_{ISC} drops to 10 Ω however, the estimation suffers from a major error build-up. This is reasonable as the drop of ISC resistance causes an enlarged current offset, which affects the transition dynamics of SOC and U_p heavily. By comparison, the proposed method, utilizing the model switching framework, converges faster with a higher steady-state accuracy. This is attributed to the timely switching to faulty cell model and continuous compensation of the R_{ISC}-induced dynamic deviation. It is also noted that the impact of capacity fading to state estimate is ignorable thanks to the voltage feedback mechanism. The accurate and degradation-robust state estimation lays a solid foundation for the ISC diagnostic.

The estimated ISC current is plotted in Fig. 8 (a-b). It is shown that all the methods converge to values close to the reference trajectory. Specifically, the ISC current is explicitly overestimated by using the SOC-based method. The SOC-based method is expected to give an unbiased I_{ISC} estimation, provided that the battery capacity is known precisely. However, the estimation is easily biased if the method is unaware of the aging status of battery. Similarly, the NCM-MS method also converges to values substantially away from the benchmarks. The observed deviation can be explained by the deficiency of normal cell model and the associated biased state estimation, which has been readily discussed in Fig. 7. By comparison, the proposed method converges much more rapidly than the reference methods. Moreover, the ISC current estimates agree more closely with the benchmarked values. The highly authentic ISC current estimation lays sound foundation for the subsequent estimates of ISC resistance.

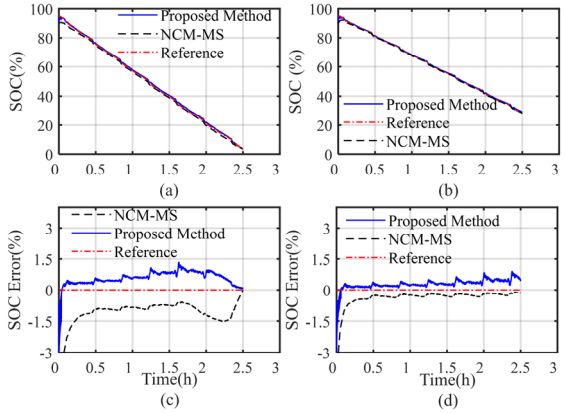

Fig. 7 SOC estimation results: (a) estimation and (b) estimation error with 10 Ω R_{ISC}; (c) estimation and (d) estimation error with 25 Ω R_{ISC}.

TABLE III
SOC Estimation Errors

	Proposed method		NCM-MS	
	10 Ω R_{ISC}	25 Ω R_{ISC}	10 Ω R_{ISC}	25 Ω R_{ISC}
MAE (%)	0.6170	0.3324	1.0934	0.3784
RMSE (%)	0.6780	0.3852	1.2455	0.6041

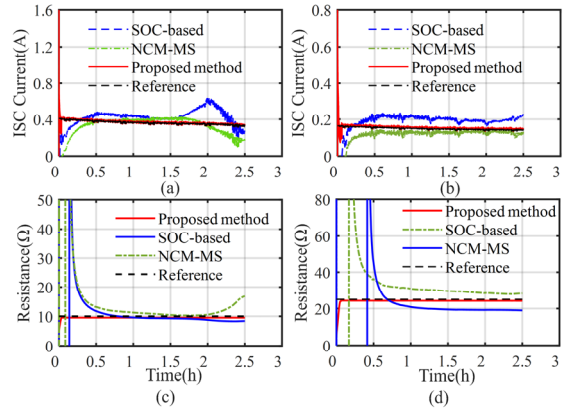

Fig. 8 Fault diagnostic results: (a) I_{ISC} estimates with 10 Ω R_{ISC}; (b) I_{ISC} estimates with 25 Ω R_{ISC}; (c) R_{ISC} estimates with 10 Ω R_{ISC}; (d) R_{ISC} estimates with 25 Ω R_{ISC}.

The ISC resistance estimation results are plotted in Fig. 8 (c-d), while the MAE and RMSE of ISC resistance estimation are summarized in Fig. 9. It is observed that the R_{ISC} estimates converge fast from the large initialization offset and follows the reference values accurately by using the proposed method. The MAE and RMSE of R_{ISC} estimation are less than 0.5 Ω and 1 Ω, which is sufficiently small referring to their baseline values of 10 Ω and 25 Ω. In contrast, the two reference methods exhibit large fluctuations at the start-up stage and converge after a long transition period of 2000 s. Moreover, the converged estimates deviate substantially from the reference values especially for the case of 25 Ω ISC resistance. The MAE and RMSE reach up to 5 Ω, corresponding to a large mismatch of around 20%. These findings are in accordance with the estimation results of ISC current as observed in Fig. 8 (a-b).

Summarily, the proposed method promises a two-fold benefit. First, the R_{ISC} estimation based on multi-state fusion is less sensitive to the capacity, thus enables a higher robustness to the battery aging. Second, the model switching architecture circumvents the co-estimation of cross-interfaced variables, and gives an encouraging converging/steady-state performance.

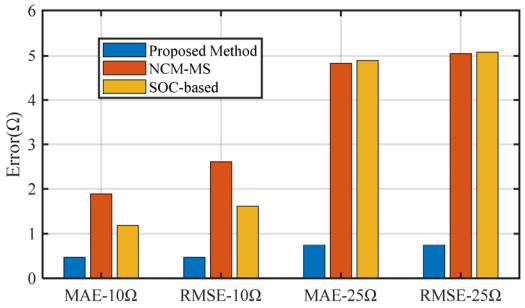

Fig. 9 MAE and RMSE of R_{ISC} estimation.

C. Validation of Disturbance Immunity

Random noises with standard deviation of 10 mA and 4 mV are added to the measurements to represent a noise-corrupted working condition. The proposed method is further compared with its RLS-based counterpart to give a direction illustration. The comparison is insightful as the LS is most progressively-used method for solving the discussed regression problem, and has been used frequently for ISC diagnostic [16, 17, 19].

The estimation results are shown in Fig. 10. As the noise corruption on system input and output violates the underlying assumption of LS principle, the RLS-based method gives rise to R_{ISC} estimates substantially away from the ground truth. This deviation, in return, feedbacks via the close-loop architecture and shares the responsibility of the overestimated offset of I_{ISC} estimation. By comparison, the estimates with the proposed method approach the benchmark much more tightly. This is attributed to the efficient compensation of noise effect, which eventually mitigates the estimation biases on the unknowns. It is also worth noting that the estimates, especially for the case of RLS-based counterpart, suffer from marked error build-up as the R_{ISC} becomes larger. The growing vulnerability to R_{ISC} is explained by that a large R_{ISC} equals to a small I_{ISC}, which leads to a low signal-noise ratio. Overall speaking however, the well-kept estimation accuracy testifies about the strong robustness of proposed method to the disturbances from data acquisition.

The MAE and RMSE of the experimental estimation results are tabulated in Table III. By comparing with the simulation results in Table I, it is easy to draw the conclusion that the proposed method has a deteriorative performance. This is within expectation as the practical experiments incur large uncertainties from multiple processes, like the model limitation, the SOC-OCV fitting error, the model parameter deviation, and the capacity fade.

To further justify the noise immunity of the proposed method, the estimation results of ISC resistance under a sweeping range of noise standard deviations are plotted in Fig. 11. Particularly, the standard deviation of noise on terminal voltage varies from 0 to 8 mV, while that on load current changes from 0 to 0.2 A proportionally. As depicted in Fig. 11, the proposed method and its RLS-based counterpart perform equivalently with high precision under the low noise scenario. With the growth of noise intensity, the RLS-based method suffers from a substantial and monotonous loss of accuracy, while the performance of the proposed method deteriorates quite slightly. Attributed to the bias elimination mechanism, the proposed method manifests itself with a high fidelity even if large noises are participated. The universal merit of high accuracy verifies that the previous conclusion about noise immunity is non-trivial, and the RTLS algorithm outperforms the widely-used RLS-based method in terms of the immunity to disturbances. Again, the accurate estimation of R_{ISC} directly validates the capability of the proposed method in diagnosing the severity of ISC fault.

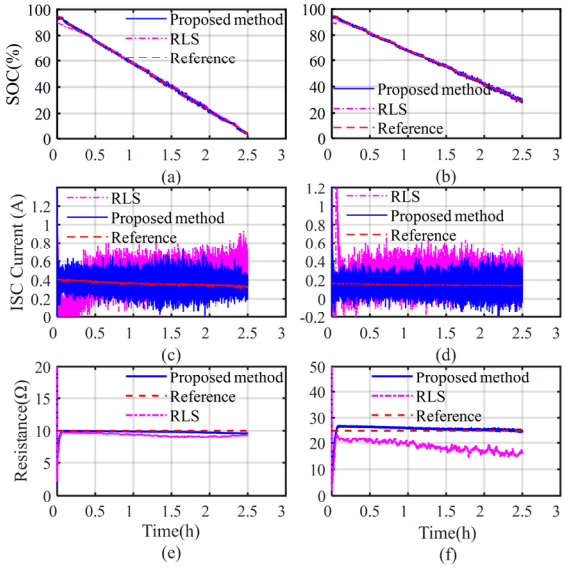

Fig. 10 Experimental results with measurement noises: SOC estimation with (a) 10 Ω R_{ISC}, and (b) 25 Ω R_{ISC}; ISC current estimation with (c) 10 Ω R_{ISC}, and (d) 25 Ω R_{ISC}; ISC resistance estimation with (e) 10 Ω R_{ISC}, and (f) 25Ω R_{ISC}.

TABLE IV
MAE AND RMSE OF R_{ISC} ESTIMATION WITH MEASUREMENT NOISES

	MAE	RMSE
10 Ω RTLS	0.3922 Ω	0.4044 Ω
10 Ω RLS	0.6708 Ω	0.7080 Ω
25 Ω RTLS	0.8673 Ω	0.9432 Ω
25 Ω RLS	6.2011 Ω	6.4970 Ω

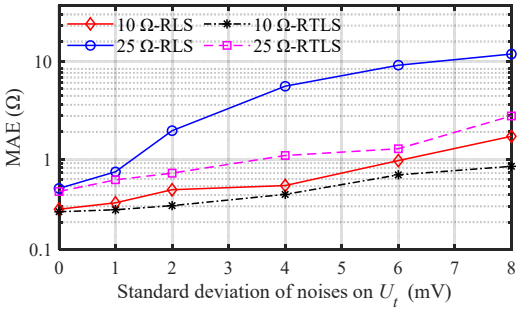

Fig. 11 Estimation results of ISC resistance under a sweeping range of noise standard deviations.

A prolonged experiment is performed to validate the stability of the proposed method. The test battery is discharged from 95%

SOC to 10% SOC using the FUDS current profile, and then charged to 95% SOC with 1/3 C current. This process is repeated for eight times, giving rise to a total testing time of 60 h. The measured current and terminal voltage are plotted in Fig. 12 (a-b), while the estimation results of I_{ISC} and R_{ISC} are plotted in Fig. 12 (c-d). As can be seen, the ISC current is estimated accurately with the errors confined within the ± 0.04 A error bound. Despite the large initialization error, the R_{ISC} estimates converge to the benchmarked values fast and precisely. The estimation errors are well within the ± 0.5 Ω bounds, and the MAE of R_{ISC} estimation is as small as 0.3523 Ω. All these clues validate that the proposed method has sufficient accuracy and stability in diagnosing the ISC fault in a long-term manner.

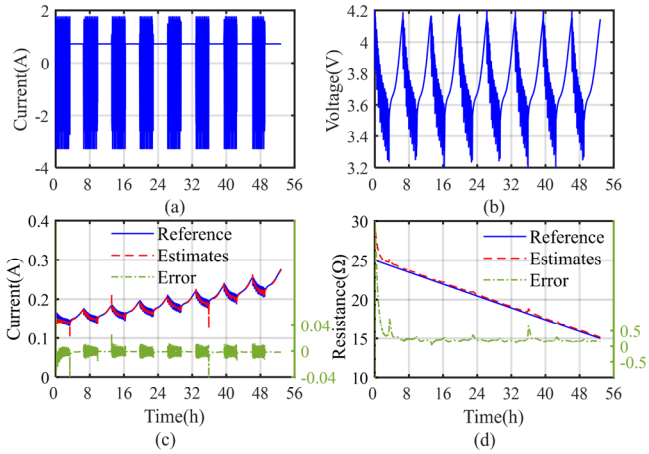

Fig. 12 Prolonged Experimental results: (a) Measured current profile, (b) Measured voltage profile, (c) I_{ISC} estimates, (d) RISC estimates.

D. Computational Tractability

The real-time performance of algorithm on the target MCU is straightforward to measure the computing complexity. After compiling, the target machine code size is 158 kilobytes, which is much less than the memory of MPC5554. The average calculation load rate is 25.83% for executing the proposed method. Therefore, the computational burden of the proposed method can be satisfied by the MPC5554-embeded MCU.

The absolute CPU time per execution is straightforward to evaluate the computational tractability. The algorithms are tested on a laptop with 3.4 GHZ CPU and 32.0 G DRAMs, and the consumed CPU times are listed in Table V. Due to the lower computational complexity of RLS, the RLS-based method shows shorter CPU time than the former three methods utilizing the RTLS algorithm. By comparison, the proposed method needs 17.32% more time than its RLS-based counterpart. It is noted that the "SOC-based" method stands for the state-of-the-art benchmark [19, 21]. Explicitly, in spite of the substantially improved fidelity, the proposed method has computational tractability comparable to the benchmarked methods.

TABLE V
COMPARATIVE RESULTS OF CPU TIME FOR DIFFERENT METHOD

	Proposed method	SOC-based	NCM-MS	RLS-based
CPU Time	15.76μs	15.01μs	14.08μs	13.03μs

E. Discussion

The ISC fault is diagnosed in real time in this paper, instead of being predicted some steps ahead. The real-time estimated ISC resistance is informative to evaluate the present severity of ISC. It can also provide a pre-warning reference for the future possibility of triggering on the thermal build-up and much more serious thermal runaway. However, there lacks a direct method to predict accurately the future evolvement of ISC, which can be an important topic for the future work.

The proposed method is affected by the battery temperature. First, the impedance parameters are linked to the temperature. This can be compensated by building a parameter-temperature dependence via look-up table or empirical equations [39]. Second, the SOC-OCV function is temperature dependent, which however can be addressed by building a multi-dimensional map among the SOC, temperature, and OCV [40]. The proposed method can hence be extended easily to include the temperature effect in a similar manner.

The proposed method can be theoretically generalized to other types of LIBs, provided that the battery dynamics can be modeled accurately. The widely-used LiNMC and $LiFePO_4$ batteries have been validated to be modeled accurately by the first-order RC model in use [41]. However, it is known that the $LiFePO_4$ battery exhibits a flatter SOC-OCV curve [40]. This potentially causes a quasi-observable condition that may decline the SOC estimation accuracy. Considering that the SOC is a critical intermediate variable, it is expected that the proposed method, albeit applicable, will suffer from a drop of accuracy inevitably on the $LiFePO_4$ battery.

The proposed method is aimed ultimately to be embedded in a cell-level processor to enable developing the self-regulated smart battery. Particularly, each cell within the pack is devised with a cell processor for monitoring and controlling. In this way, the system management can be realized in a distributed fashion. The self-organized smart battery system can offer large superiorities of high modularity, high scalability, and enhanced fault tolerance. This emerging technique is also depicted in BATTERY 2030+ Roadmap of Europe.

It is worth noting that the proposed method is also applicable to the widely-used battery management system, where the cell current and voltage are sent to the master or slave controller for monitoring and control. A challenge is the improved computing burden for diagnosing many cells simultaneously. There can be two solutions to mitigate this challenge. First, a slave controller can be devised for each battery module, so that the computing burden can be distributed to several affordable portions for localized diagnostic. Second, an extra screening can be added before using the cell voltage abnormality. The hierarchical scheme can largely lower down the computing burden.

VI. CONCLUSION

This paper proposes an aging-robust and disturbance-immune ISC diagnostic method for the LIB. The method incorporates a multi-state-fusion ISC resistance estimator and a RTLS-VF-based bias compensator within a universal model-switching

framework. Simulations and experiments have been performed for validation in terms of the diagnostic accuracy, as well as the robustness to battery aging and noise corruption. The primary conclusions are summarized as follows:

(1) The ISC diagnostic is robust to the battery aging. The ISC resistance is estimated accurately with the MAE confined to 0.5 Ω and 1 Ω for the case of 10 Ω and 25 Ω ISC resistance.

(2) The high diagnostic accuracy is rooted in the precise state estimate. It is validated that the SOC and ISC current have been estimated authentically with error of 0.617% and 0.3324%.

(3) The proposed method outperforms the state-of-the-art techniques in the noise immunity. The MAE of ISC resistance estimation is constrained to 1 Ω when strong noises with standard deviation of 0.1 A and 4 mV corrupt the measurements.

REFERENCES

[1] X. Hu, C. Zou, C. Zhang, and Y. Li, "Technological Developments in Batteries: A Survey of Principal Roles, Types, and Management Needs," IEEE Power and Energy Magazine, vol. 15, no. 5, pp. 20-31, Sept.-Oct. 2017.

[2] X. Feng, M. Ouyang, X. Liu, L. Lu, Y. Xia, and X. He, "Thermal runaway mechanism of lithium ion battery for electric vehicles: A review," Energy Storage Materials, vol. 10, May 2017.

[3] K. Liu, Y. Li, X. Hu, M. Lucu, and W. D. Widanage, "Gaussian process regression with automatic relevance determination kernel for calendar aging prediction of lithium-ion batteries," IEEE Transactions on Industrial Informatics, vol. 16, no. 6, pp. 3767-3777, Jun. 2019.

[4] R. Xiong, R. Yang, Z. Chen, W. Shen, and F. Sun, "Online Fault Diagnosis of External Short Circuit for Lithium-Ion Battery Pack," IEEE Transactions on Industrial Electronics, vol. 67, no. 2, pp. 1081-1091, Feb. 2020.

[5] Y. Shang, G. Lu, Y. Kang, Z. Zhou, B. Duan, and C. Zhang, "A multi-fault diagnosis method based on modified Sample Entropy for lithium-ion battery strings," Journal of Power Sources, vol. 446, pp. 227275, Jan. 2020.

[6] D. Finegan et al., "Characterising thermal runaway within lithium-ion cells by inducing and monitoring internal short circuits," Energy Environ. Sci., vol. 10, pp. 1377-1388, Apr. 2017.

[7] P. Ramadass, W. Fang, and Z. Zhang, "Study of internal short in a Li-ion cell I. Test method development using infra-red imaging technique," Journal of Power Sources, vol. 248, pp. 769-776, Feb. 2014.

[8] A. Moeini and S. Wang, "Fast and Precise Detection of Internal Short Circuit on Li-Ion Battery," in 2018 IEEE Energy Conversion Congress and Exposition (ECCE). 2018, pp. 2759-2766, Sept. 2018.

[9] B. Xia, Y. Shang, T. Nguyen, and C. Mi, "A correlation based fault detection method for short circuits in battery packs," Journal of Power Sources, vol. 337, pp. 1-10, Jan. 2017.

[10] X. Kong, Y. Zheng, M. Ouyang, L. Lu, J. Li, and Z. Zhang, "Fault diagnosis and quantitative analysis of micro-short circuits for lithium-ion batteries in battery packs," Journal of Power Sources, vol. 395, pp. 358-368, Aug. 2018.

[11] Y. Kang, B. Duan, Z. Zhou, Y. Shang, and C. Zhang, "Online multi-fault detection and diagnosis for battery packs in electric vehicles," Applied Energy, vol. 259, pp. 114170, Feb. 2020.

[12] Z. Chen, K. Xu, J. Wei, and G. Dong, "Voltage fault detection for lithium-ion battery pack using local outlier factor," Measurement, vol. 146, pp. 544-556, Nov. 2019.

[13] X. Kong et al., "Signal synchronization for massive data storage in modular battery management system with controller area network," Applied Energy, vol. 197, pp. 52-62, Jul. 2017.

[14] Y. Zheng et al., "Cell state-of-charge inconsistency estimation for LiFePO4 battery pack in hybrid electric vehicles using mean-difference model," Applied Energy, vol. 111, pp. 571–580, Nov. 2013.

[15] M. Ouyang et al., "Internal short circuit detection for battery pack using equivalent parameter and consistency method," Journal of Power Sources, vol. 294, pp. 272-283, Oct. 2015.

[16] W. Gao, Y. Zheng, M. Ouyang, L. Jianqiu, X. Lai, and X. Hu, "Micro-Short Circuit Diagnosis for Series-Connected Lithium-Ion Battery Packs Using Mean-Difference Model," IEEE Transactions on Industrial Electronics, vol. 66, no. 3 , pp. 2132-2142, May 2018.

[17] Z. Zhang, X. Kong, Y. Zheng, L. Zhou, and X. Lai, "Real-time diagnosis of micro-short circuit for Li-ion batteries utilizing low-pass filters," Energy, vol. 166, pp. 1013-1024, Oct. 2018.

[18] X. Feng, C. Weng, M. Ouyang, and J. Sun, "Online internal short circuit detection for a large format lithium ion battery," Applied Energy, vol. 161, pp. 168-180, Jan. 2016.

[19] M. Seo, T. Goh, M. Park, G. Koo, and S. Kim, "Detection of Internal Short Circuit in Lithium Ion Battery Using Model-Based Switching Model Method," Energies, vol. 10, pp. 76, Oct. 2017.

[20] Z. Chen, R. Xiong, T. Jinpeng, X. Shang, and J. Lu, "Model-based fault diagnosis approach on external short circuit of lithium-ion battery used in electric vehicles," Applied Energy, vol. 184, pp. 365-374, Dec. 2016.

[21] T. Kim, D. Makwana, A. Adhikaree, J. Vagdoda, and Y. Lee, "Cloud-Based Battery Condition Monitoring and Fault Diagnosis Platform for Large-Scale Lithium-Ion Battery Energy Storage Systems," Energies, vol. 11, no.1 , pp. 125, Jan. 2018.

[22] Q. Ouyang, J. Chen, and J. Zheng, "State-of-Charge Observer Design for Batteries With Online Model Parameter Identification: A Robust Approach," IEEE Transactions on Power Electronics, vol. 35, no. 6, pp. 5820-5831, Jun. 2020.

[23] Y. Feng, C. Xue, Q. Han, F. Han, and J. Du, "Robust Estimation for State-of-Charge and State-of-Health of Lithium-Ion Batteries Using Integral-Type Terminal Sliding-Mode Observers," IEEE Transactions on Industrial Electronics, vol. 67, no. 5, pp. 4013-4023, May 2020.

[24] R. Zhu, B. Duan, J. Zhang, Q. Zhang, and C. Zhang, "Co-estimation of model parameters and state-of-charge for lithium-ion batteries with recursive restricted total least squares and unscented Kalman filter," Applied Energy, vol. 277, pp. 115494, Nov. 2020.

[25] Z. Yu, L. Xiao, H. Li, X. Zhu, and R. Huai, "Model parameter identification for lithium batteries using the coevolutionary particle swarm optimization method," IEEE Transactions on Industrial Electronics, vol. 64, no. 7, pp. 5690-5700, Mar 2017.

[26] Z. Wei, G. Dong, X. Zhang, J. Pou, Z. Quan, and H. He, "Noise-immune model identification and state of charge estimation for lithium-ion battery using bilinear parameterization," IEEE Transactions on Industrial Electronics, vol. 68, no.1, pp. 312-323, Jan. 2021.

[27] J. Meng, D.-I. Stroe, M. Ricco, G. Luo, and R. Teodorescu, "A simplified model-based state-of-charge estimation approach for lithium-ion battery with dynamic linear model," IEEE Transactions on Industrial Electronics, vol. 66, no. 10, pp. 7717-7727, Oct. 2019.

[28] Z. Song, J. Hou, H. F. Hofmann, X. Lin, and J. Sun, "Parameter Identification and Maximum Power Estimation of Battery/Supercapacitor Hybrid Energy Storage System Based on Cramer–Rao Bound Analysis," IEEE Transactions on Power Electronics, vol. 34, no. 5, pp. 4831-4843, May 2018.

[29] B. Xiong, J. Zhao, Y. Su, Z. Wei, and M. Skyllas-Kazacos, "State of charge estimation of vanadium redox flow battery based on sliding mode observer and dynamic model including capacity fading factor," IEEE Transactions on Sustainable Energy, vol. 8, no. 4, pp. 1658-1667, Oct. 2017.

[30] Z. Wei, J. Zhao, D. Ji, and K. J. Tseng, "A multi-timescale estimator for battery state of charge and capacity dual estimation based on an online identified model," Applied energy, vol. 204, pp. 1264-1274, Oct. 2017.

[31] X. Lin, "Theoretical Analysis of Battery SOC Estimation Errors Under Sensor Bias and Variance," IEEE Transactions on Industrial Electronics, vol.65, no.9, pp. 7138-7148, Jan. 2018.

[32] T. Kim, Y. Wang, Z. Sahinoglu, T. Wada, S. Hara, and W. Qiao, "A Rayleigh Quotient-Based Recursive Total-Least-Squares Online Maximum Capacity Estimation for Lithium-Ion Batteries," IEEE Transactions on Energy Conversion, vol. 30, no. 3, pp. 1-10, Sept. 2015.

[33] Z. Wei, C. Zou, F. Leng, B. Soong, and K. Tseng, "Online model identification and state of charge estimate for lithium-ion battery with a recursive total least squares-based observer," IEEE Transactions on Industrial Electronics, vol. 30, no.3, pp. 842-851, Sept. 2017.

[34] R. Arablouei, S. Werner, and K. Doğançay, "Analysis of the gradient-descent total least-squares adaptive filtering algorithm," IEEE Transactions on Signal Processing, vol. 62, no. 5, pp. 1256-1264, Mar. 2014.

[35] Z. Wei, D. Zhao, H. He, W. Cao, and G. Dong, "A noise-tolerant model parameterization method for lithium-ion battery management system," Applied Energy, vol. 268, pp. 114932, Jun. 2020.
[36] A. Hauser and R. Kuhn, "High-voltage battery management systems (BMS) for electric vehicles," in Advances in Battery Technologies for Electric Vehicles: Elsevier, 2015, pp. 265-282.
[37] L. Lu, X. Han, J. Li, J. Hua, and M. Ouyang, "A review on the key issues for lithium-ion battery management in electric vehicles," J Power Sources, vol. 226, pp. 272-288, Mar. 2013.
[38] L. Liu et al., "Comparative study on substitute triggering approaches for internal short circuit in lithium-ion batteries," Applied Energy, vol. 259, pp. 114143, Feb. 2019.
[39] J. Gomez, R. Nelson, E. E. Kalu, M. H. Weatherspoon, and J. P. Zheng, "Equivalent circuit model parameters of a high-power Li-ion battery: Thermal and state of charge effects," Journal of Power Sources, vol. 196, no. 10, pp. 4826-4831, May. 2011.
[40] W. Zhang, W. Shi, and Z. Ma, "Adaptive unscented Kalman filter based state of energy and power capability estimation approach for lithium-ion battery," Journal of Power Sources, vol. 289, pp. 50-62, Sept. 2015.
[41] X. Hu, S. Li, and H. Peng, "A comparative study of equivalent circuit models for Li-ion batteries," Journal of Power Sources, vol. 198, pp. 359-367, Jan. 2012.

Jian Hu received the B.S. degree in automotive engineering from the Beijing Institute of Technology, Beijing, China, in 2019. He is currently working toward the M.S. degree in mechanical engineering at Beijing Institute of Technology, Beijing, China.

His research interests include the battery state estimation and fault diagnosis.

Hongwen He (M'03–SM'12) received the M.Sc. degree from Jilin University of Technology, Changchun, China and the Ph.D. degree from Beijing Institute of Technology, Beijing, China, in 2000 and 2003, both in vehicle engineering.

He is currently a Professor with the National Engineering Laboratory for Electric Vehicles, School of Mechanical Engineering, Beijing Institute of Technology. He has published 126 EI-indexed papers, 82 SCI-indexed papers, and 17 ESI highly cited papers. He has been awarded the second prize of the Chinese National Science and Technology Award, the first prize of natural science by the Ministry of Education, the first prize of technological invention of China's automobile industry and the second prize of national defense technology.

Zhongbao Wei (M'19, 94433453) received the B.Eng. and the M.Sc. degrees in instrumental science and technology from Beihang University, China, in 2010 and 2013, and the Ph.D. degree in power engineering from Nanyang Technological University, Singapore, in 2017.

He has been a research fellow with Energy Research Institute @ NTU, Nanyang Technological University from 2016 to 2018. He is currently a Professor in vehicle engineering with the National Engineering Laboratory for Electric Vehicles, School of Mechanical Engineering, Beijing Institute of Technology, China. He has authored more than 60 peer-reviewed articles. His research interests include battery management and energy management for hybrid energy systems. He is an Associate Editor for the journal of IET renewable power generation and IET intelligent transportation. He is a Guest Editor of IEEE Journal of Emerging and Selected Topics in Power Electronics.

YANG LI (S'11–M'16) received the B.E. degree in electrical engineering from Wuhan University, Wuhan, China, in 2007, and the M.Sc. and Ph.D. degrees in power engineering from the Nanyang Technological University (NTU), Singapore, in 2008 and 2015, respectively. From 2015 to 2016, he was a Research Fellow with the Energy Research Institute at NTU (ERI@N), Singapore. From 2016 to 2018, he was a Research Fellow with the School of Electrical Engineering and Computer Science, Queensland University of Technology, Brisbane, Australia. Since 2019, he has been an Associate Professor with School of Automation, Wuhan University of Technology, Wuhan, China. He is currently a Researcher with the Department of Electrical Engineering, Chalmers University of Technology. His research interests include modeling, control, and application of renewable and energy storage systems in power grid and transport sectors. Dr. Li was a recipient of the EU Marie Skłodowska-Curie Individual Fellowship in 2020.